Reynolds number scaling of grid-point requirements of wall-modeled large eddy simulation of separated flows

By R. Agrawal, S. T. Bose† AND P. Moin

1. Motivation and objectives

In complex engineering flows, the boundary layers over solid surfaces often experience a combination of favorable and adverse pressure gradients. A favorable pressure gradient reduces the normal stresses in the near-wall flow, making it more organized (Sreenivasan 1982). In the presence of an adverse pressure gradient, however, the normal stresses near the wall become stronger (Adams & Johnston 1988). For three-dimensional flows, the problem is further complicated by the lack of uniformity in any spatial direction. These nonequilibrium flows can even exhibit a boundary layer separation from the surface before finally reattaching downstream. The structure of turbulent separation bubbles has remained a matter of active research (Lighthill 1953; Kiya & Sasaki 1983; Adams & Johnston 1988). Even in canonical problems of boundary layers experiencing pressure gradients without separating off the surface, integrated streamwise history effects have been reported (Bobke *et al.* 2017) to determine the downstream state of a boundary layer. Recently, Agrawal *et al.* (2023*a*) developed an extension of the Thwaites method which also serves as a quantitative analysis tool to account for the flow history. For example, in the flow over an aircraft model, a different pressure gradient distribution can occur for different angles of attack due to inviscid effects that can change the resulting effective body shape. The changes in the angle of attack lead to variations in the physical effects that drive the grid point requirements for converging the quantities of interest (such as lift, pitching moments, drag, surface pressure, etc). As an example, existing results from wall-modeled LES (WMLES) for the flow over the Common Research Model aircraft (Agrawal *et al.* 2023*c*; Kiris *et al.* 2022; Goc *et al.* 2023; Kiris *et al.* 2023) have demonstrated that converging the predictions (of the pitching moment) from simulations at the higher angles of attack (near, at, and post-stall regions) is more challenging than at the lower angles of attack where the flow is primarily attached.

Detailed knowledge of the near-wall structure of equilibrium boundary layers has been leveraged to establish resolution requirements for both wall-resolved and wall-modeled large-eddy simulations (e.g., $\Delta u_\tau/\nu \sim O(1)$ for wall-resolved LES or the validity of the law of the wall in the logarithmic regions of the velocity profiles in WMLES). Despite the augmentation of the structure of the turbulent boundary layer in the presence of strong pressure gradients, existing grid point estimates still rely on the phenomenology of equilibrium boundary layers (Chapman 1979; Choi & Moin 2012; Yang & Griffin 2021). These studies suggest that the grid point requirements for WMLES scale linearly with the Reynolds number if resolution with respect to the boundary layer remains fixed. There are two shortcomings of this approach. First, the conclusions regarding the Reynolds number scaling may be incorrect in the presence of pressure gradients. Second,

and perhaps more importantly, the existing grid point estimates do not provide estimates on the *a-posteriori* errors in quantities of interest given a specified outer layer resolution. For instance, Lozano-Durán *et al.* (2022) show that errors in the prediction of mean velocity profiles greatly increase in regions of adverse pressure gradients compared to zero pressure gradient regions even if the outer layer resolution is fixed. This is especially true in separating boundary layers, where significantly higher outer layer resolution has been required for accurate simulations (Whitmore *et al.* 2022).

This brief aims to address the aforementioned shortcomings in the context of separating flows. A characteristic length scale that governs the near-wall flow equilibrium (a quasi-balance between the viscous and the pressure gradient terms) is used to determine the resolution required for accurately predicting quantities of interest for flows (such as the surface pressure) that exhibit a smooth body separation across a range of Reynolds numbers. For these purposes, we utilize the charLES flow solver (Brès *et al.* 2018) to perform WMLES. The rest of the brief is organized as follows. Section 2 provides some details of the charLES flow solver. Section 3 discusses the physical length scale that governs the prediction of smooth body separation. Section 4 discusses *a-posteriori* WMLES results across multiple flows. Finally, some conclusions are drawn in Section 5.

2. Solver and wall modeling details

The simulations presented in this work are performed using charLES, an explicit, unstructured, finite-volume solver for the compressible Navier-Stokes equations. This code is formally second-order accurate in space and third-order accurate in time, and utilizes grids based on Voronoi diagrams. The dynamic tensor coefficient Smagorsinky model developed in Agrawal *et al.* (2022) has been used in this study. More details of the solver and validation cases can be found in Agrawal *et al.* (2023b); Brès *et al.* (2018); Goc *et al.* (2021); Fu *et al.* (2021). Formally skew-symmetric operators are employed to conserve kinetic energy in the and the discrete operators also approximately preserve entropy in the inviscid, adiabatic limit.

In typical WMLES, a shear stress and a heat flux boundary value is supplied to the LES solver to close the discrete system of governing equations. In this work, an algebraic form of the equilibrium wall-stress model (EQWM) is used, in which the assumed mean velocity profile is a C^1 continuous piecewise fit of the viscous sublayer and the logarithmic layer. Details of the compressible formulation of the EQWM can be found in Lehmkuhl *et al.* (2018). A first-point matching approach is used, since this solver has not shown any evidence of a log-layer mismatch in the simulation of turbulent channel flows in the range, $1000 \le Re_\tau \le 4200$ with typical LES resolutions.

3. A characteristic length scale for separated flows

Fundamentally, even the viscously driven near-wall scales in flows experiencing pressure gradients can go out of equilibrium (for example, not have a linear velocity scaling in viscous units) if the timescale governed by the pressure gradient ($t_p \sim \rho u_\tau/dP/dx$) is faster than the viscous timescale ($t_v \sim \nu/u_\tau^2$), where u_τ is the local skin-friction velocity. The timescale for eddies within a logarithmic region is governed by the local shear ($t_{iv} \sim h/u_\tau$). Thus the inner scales thus go out of equilibrium if

$$t_p \ll t_v \text{ or } u_\tau^3 \ll \frac{\nu}{\rho}\frac{dP}{dx} = (u_p)^3. \tag{3.1}$$

Similarly, both the inner and outer scales respond at the same timescale if

$$t_p \ll t_v \sim t_{iv} \text{ or } \frac{u_p}{u_\tau} \gg 1 \text{ and } \frac{u_\tau h}{\nu} \sim 1. \tag{3.2}$$

Near the onset of flow separation, these conditions can be met simultaneously. For a spatially developing boundary layer, these relations also suggest that the flow at a given wall-normal location h is bound to be in nonequilibrium if

$$\frac{u_p h}{\nu} \gg 1 \text{ or } \frac{h}{l_p} \gg 1 \text{ where } l_p = \frac{\nu}{u_p}. \tag{3.3}$$

Thus, the only scales that remain in equilibrium for a boundary layer before the onset of a separation bubble are scaled such that $\frac{h}{l_p} \sim 1$. This suggests that an equilibrium wall model approximation would only remain valid for matching locations at $h \lesssim \alpha l_p$ (for some constant, α).

This can be further reasoned from analysis of a time-steady Poisson equation near the separation point, written as

$$\langle \rho \frac{\partial \bar{u}_i}{\partial x_j} \frac{\partial \bar{u}_j}{\partial x_i} \rangle = -\nabla^2 \langle \bar{p} \rangle, \tag{3.4}$$

where $\bar{\cdot}$ and $\langle \cdot \rangle$ denote the filtered LES fields and a time average operator, respectively, and homogeneous Neumann boundary conditions are applied on the pressure field at the solid wall (see 2). Consider, in Figure 2, a two-dimensional boundary layer that undergoes a separation over a surface such that $\delta/R \ll 1$ where R is the local radius of curvature. (This assumption is not strictly true near the separation point, but is convenient for analysis.) Let $(x_{sep}, 0)$ be the coordinates of the separation point. In a semi-infinite domain such as in Figure 2, the Green's function that satisfies Eq. (3.4) and its boundary conditions is given as

$$G(x, y, x_0, y_0) = \frac{1}{4\pi} ln([(x - x_0)^2 + (y - y_0)^2][(x - x_0)^2 + (y + y_0)^2]). \tag{3.5}$$

for $y \geq 0$.

Using Green's identities and the symmetric property of Green's function, the pressure in the upper-half domain is given as

$$p_{sep}^* = p^*(x_{sep}, 0) = -\int_0^\infty \int_{-\infty}^\infty \frac{\rho}{2\pi} ln((x^* - x_{sep}^*)^2 + (y^*)^2) \frac{\partial u_i^*}{\partial x_j^*} \frac{\partial u_j^*}{\partial x_i^*} dx^* dy^*, \tag{3.6}$$

where $(...)^*$ denotes a nondimensional variable, and the $\langle \cdots \rangle$ has been dropped for simplicity. Let the relevant scales for nondimensionalization be $l_{min} = min(l_p(x))$ and the viscous velocity scale that corresponds to l_{min}, equal to $u_{max} \approx \nu/l_{min}$. Under this normalization, let L_p^{M*} be the scale of the region that dominantly influences the pressure at the separation point. For this region to be of a finite length scale, the integrand must decrease eventually, or

$$(L_p^{M*})^2 \frac{\partial u_i^*}{\partial x_j^*} \frac{\partial u_j^*}{\partial x_i^*} \lesssim \Lambda^2, \tag{3.7}$$

where some finite Λ. For an LES, one of the aims is to find the minimum L_p^{M*} that needs to be resolved on the computational grid to accurately predict separation. The minimum
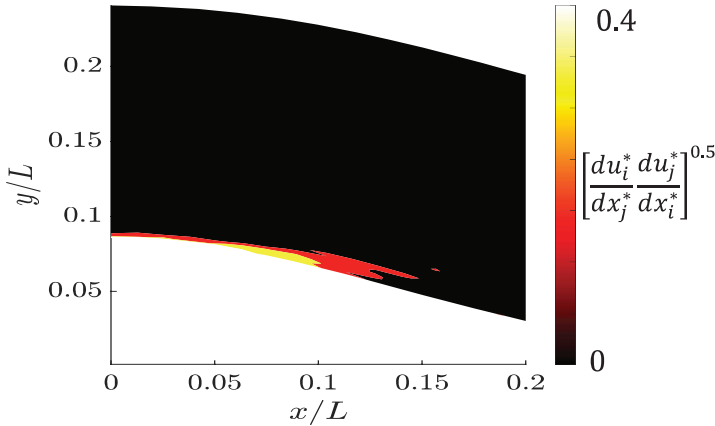
FIGURE 1. A two-dimensional (spanwise and time-averaged) contour of $du_i/dx_j du_j/dx_i$ in the vicinity of the separation point ($x/L = 0.1$) for the flow over the Boeing speed bump.

L_p^M that would always satisfy the above inequality is one that also satisfies

$$(L_p^{M*})^2 \le \frac{\Lambda^2}{max\{\frac{\partial u_i^*}{\partial x_j^*}\frac{\partial u_j^*}{\partial x_i^*}\}}. \tag{3.8}$$

Stratford (1959) suggests that at the points where the skin friction crosses a zero, the near-wall velocity profile (up to $y^+ = \frac{u_\tau y}{\nu} = 5 - 10$) is given as

$$\frac{u}{u_p} = A + B\sqrt{y_p} = A + B\sqrt{\frac{yu_p}{\nu}}. \tag{3.9}$$

Further assuming that near the separation point, the scales of motion in the streamwise and the wall-normal direction scales similarly

$$\max\{\frac{du_i^*}{dx_j^*}\frac{du_j^*}{dx_i^*}\} \sim \mathcal{O}(1), \tag{3.10}$$

near the wall, as the flow nears separation. This implies that

$$L_p^M \sim \chi \, l_{min} \text{ where } \chi \sim \Lambda. \tag{3.11}$$

or that a reasonable length scale that may affect a flow nearing separation is the one that is viscously scaled by the strongest adverse pressure gradient in the vicinity of the separation. As a numerical example of the analysis above, we consider the flow over the Boeing speed bump (Uzun & Malik 2022). A highly resolved WMLES (with the matching location as low as $\Delta x^+ = \Delta y^+ = \Delta z^+ = 5$ at the wall with an equilibrium wall model) was performed in-house. Whitmore *et al.* (2022) showed that the skin-friction and the surface-pressure coefficients are accurately predicted on this grid at $Re_L = 2 \times 10^6$. The resulting distribution of the product, $\sqrt{\frac{du_i}{dx_j}\frac{du_j}{dx_i}}$, is plotted in Figure 1. The maximal value is ≈ 0.4, implying $L_p^M \sim \mathcal{O}(1)$.

The value of χ may vary depending on the flow; however, this will not affect the scaling $L_p^M \sim l_{min}$. Some reasonable estimates of Λ are explored through *a-priori* analysis in the next subsection. A further implication of this fact can be that the response of the near-wall flow in the vicinity of a separation bubble can also be governed by a stronger
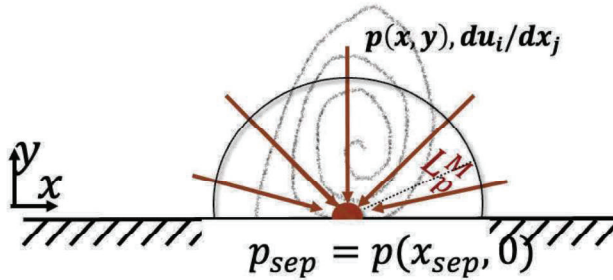
FIGURE 2. Schematic of a simplified, two-dimensional boundary layer flow where $(x_{sep}, 0)$ is the separation point. The hemisphere of radius L_p^m denotes the region that significantly influences the pressure at the separation point (assumed to be quasi-steady in time).

adverse pressure gradient upstream (locally close to the point of separation, however) of this region.

3.1. *A-priori analysis*

In this section, *a-priori* analysis is performed to explore an estimate of the expected values of Λ in nonequilibrium boundary layers. The objective is to find reasonable Λ values that provide monotonically converging and fairly accurate (for example, $\leq 10\%$ error) estimates of the wall shear stress for nonequilibrium flows. The equilibrium wall model is used for providing the estimates of the modeled wall stress. For these purposes, a high-fidelity database consisting of the adverse pressure-gradient boundary layers of Bobke *et al.* (2017) and the flow over NACA 0012 and 4412 airfoils (Vinuesa *et al.* 2018; Tanarro *et al.* 2020) is examined. A momentum-thickness-based Reynolds number (Re_θ) up to approximately 4000 and a Clauser parameter value ($\beta = \delta^*/\rho u_\tau^2 \, dP/dx$) of up to 6 is observed on these flows.

In Figures 3 and 4, the value of χ decreased from 25 to 6. For both these figures, subplot (a) denotes the location of the matching point (y_w^+) in friction units with the ordinate and the abcissa denoting the local Clauser parameter and the momentum-thickness-based Reynolds number. Similarly, subplot(b) for both the aforementioned figures presents the percentage error in the prediction of the shear stress. In Figure 3, the error in the prediction of the shear stress, τ_w, reaches up to approximately 20%, with the error generally increasing for a higher y_w^+, except when the Reynolds number is low. Generally, at a given Re_θ, the error in the shear-stress predictions increases with increasing β. This is expected, as for a larger β, a large range of the flow scales within the boundary layer are under nonequilibrium. A turbulent channel flow analog of this argument can be found in Lozano-Durán *et al.* (2020). At a given β, the increase in Re_θ generally leads to a lower error as the scale separation between the equilibrium and nonequilibrium regions of the boundary layer increases. Upon refinement in Figure 4, by reducing χ to 6 (equivalent to quadrupling the resolution), the errors are generally lower than those at $\chi = 25$. The errors for all the streamwise stations in the considered flows are less than 10% in this limit. Given the relatively modest Re_θ of these flows, the corresponding y_w^+ values are also small. However, based on these *a-priori* results, it is hypothesized that a value of $\chi \in [5, 10]$ may be necessary to accurately predict quantities of interest in *a-posteriori* WMLES of nonequilibrium flows.
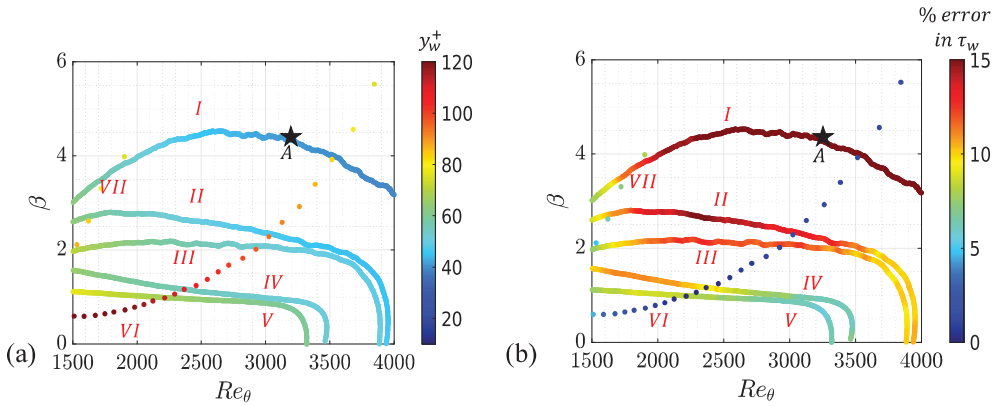
FIGURE 3. The distribution of the (a) location of the matching point in wall units (y_w^+) and (b) the corresponding percentage error in the prediction of the wall shear stress from the equilibrium wall model for $\chi = 25$ as a function of the Clauser parameter and the momentum thickness Reynolds numbers. The Roman numerals denote the data points from different flows: Data series I to V correspond to different streamwise stations in the flat-plate boundary layers simulated in Bobke *et al.* (2017). Data series VI and VII correspond to different streamwise stations in NACA 0012 and 4412 airfoils studied by Tanarro *et al.* (2020) and Vinuesa *et al.* (2018) respectively. The starred point, A, is a sample point chosen to aid the interpretability of this plot. This data point corresponds to a flat-plate boundary layer flow at $Re_\theta \sim 3200$ and $\beta = 4.2$. The matching location for this point is roughly, $y_w^+ \approx 40$ [in subfigure (a)] and the percentage error in the shear-stress prediction is approximately 20% [and hence the contour is saturated in subfigure (b)].
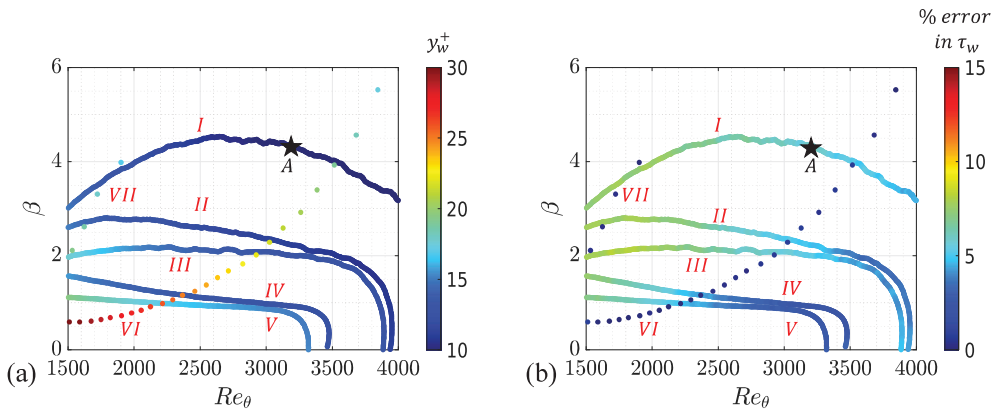

FIGURE 4. The distribution of the (a) location of the matching point in wall units (y_w^+) and (b) the corresponding percentage error in the prediction of the wall shear stress from the equilibrium wall model for $\chi = 25$ as a function of the Clauser parameter and the momentum thickness Reynolds numbers. The Roman numerals denote the data points from different flows: Data series I to V correspond to different streamwise stations in the flat-plate boundary layers simulated in Bobke *et al.* (2017). Data series VI and VII correspond to different streamwise stations in NACA 0012 and 4412 airfoils studied by Tanarro *et al.* (2020) and Vinuesa *et al.* (2018) respectively. The starred point, A, is a sample point chosen to aid the interpretability of this plot. This data point corresponds to a flat-plate boundary layer flow at $Re_\theta \sim 3200$ and $\beta = 4.2$. The matching location for this point is roughly, $y_w^+ \approx 10$ [in subfigure (a)] and the percentage error in the shear-stress prediction is approximately 6% [in subfigure (b)].
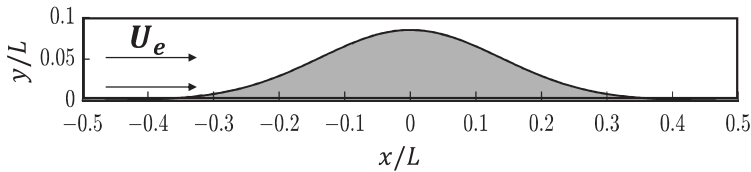
FIGURE 5. A schematic of the flow over the simplified, spanwise periodic Boeing speed bump geometry. The flow develops over a Gaussian-shaped bump experiencing a favorable and an adverse pressure gradient before eventually separating at $x/L \approx 0.1$.

3.2. *Reynolds number scaling*

The currently accepted zero-pressure-gradient flow-based estimates (Choi & Moin 2012; Yang & Griffin 2021) suggest that the number of grid points (N_{cv}) required to perform WMLES of a boundary layer scale as $N_{cv} \sim Re^1$. Instead, in this work, we propose an alternate grid-point scaling for nonequilibrium flows, specifically those that exhibit a turbulent separation. These estimates will be verified in *a-posteriori* calculations in subsequent sections. The assumption in this work is that a nearly constant value of χ, or a viscously driven length scale, can be chosen to predict the quantities of interest as the Reynolds number is increased. The value of L_p^M scales as

$$L_p^M \sim \chi l_{min} \sim \chi Re^{-2/3} \max \left(\frac{1}{\rho} \frac{dP}{dx} \right)^{-1/3}, \qquad (3.12)$$

or as the Reynolds number is increased, L_p^M decreases as $Re^{-2/3}$. Thus, for a nested grid where the number of points in the wall-normal direction with respect to L_p^M is fixed, the number of grid points required to sufficiently resolve the nonequilibrium effects scales as $N_{cv} \sim Re^{4/3}$. This prediction is more stringent than the equilibrium flat-plate boundary layer WMLES estimates but grows slower than $N_{cv} \sim Re^{13/7}$ scaling of wall-resolved LES. The assumption of requiring a fixed χ across a range of Reynolds numbers may be negated once improved wall models consistently and accurately account for the nonequilibrium and the flow history effects at coarse resolutions. (In Appendix I, the performance of some existing nonequilibrium wall models is reported, which suggests that present nonequilibrium models do not affect the resolution requirements significantly).

4. A-posteriori analysis

4.1. *WMLES of the Boeing speed bump*

In this section, *a-posteriori* results from WMLES of the flow over the Boeing speed bump (Williams *et al.* 2020; Gray *et al.* 2021, 2022) are presented. This geometry was proposed by the Boeing Company and Williams *et al.* (2020) to challenge the ability of computational fluid dynamics practices to accurately predict turbulent flow separation. Zhou *et al.* (2023) recently showed a large sensitivity in the prediction of the separation bubble to the choice of the subgrid-scale and wall models. The simplified, spanwise-periodic bump surface is defined by an analytical expression, $h(x)$, written as

$$y \left(\frac{x}{L} \right) = 0.085 \, exp \left[- \left(\frac{x}{0.195L} \right)^2 \right], \qquad (4.1)$$

where x is the streamwise coordinate. The Reynolds number, Re_L, for this flow, is defined

Mesh	N_{cv} (in millions)	Max. Δ/L	Min. Δ/L
Coarse	3	0.01	1.3×10^{-3}
Medium	12	0.01	6.3×10^{-4}
Fine	52	0.01	3.1×10^{-4}

TABLE 1. Mesh parameters for the $Re_L = 2 \times 10^6$ case of the flow over the spanwise-periodic Boeing speed bump. For subsequently higher Reynolds numbers, the grid is refined by modifying the background resolution (equal to max. Δ/L) by a factor of $Re^{2/3}$.

in terms of the freestream velocity U_∞ and the bump width L. It has been previously shown that the surface pressure (C_p) and the skin friction (C_f) for the simplified geometry approximately match those at the midspan of the experimental configuration (Gray *et al.* 2021). A Reynolds number, $Re_L = 2 \times 10^6$, is studied to match the prior quasi-DNS (Uzun & Malik 2022) and experimental results (Williams *et al.* 2020; Gray *et al.* 2021). The flow over the speed bump experiences a strong favorable pressure gradient followed by a strong adverse pressure gradient on the fore and aft sections of the bump, respectively. For $Re_L \geq 1.8 \times 10^6$, these pressure gradients lead to the formation of a turbulent separation bubble.

Figure 5 represents a schematic of the simulation setup. The inlet is located at $x/L = -1.0$ as a plug-flow profile, and the flow then undergoes a numerically induced transition to turbulence over the region ($-1.0 < x/L < -0.6$). This simple choice stems from the observations of Agrawal *et al.* (2023*a*), who showed that the separation tendency of this flow is approximately independent of the inlet boundary condition as long as the inlet is sufficiently far away. This has also been reported in *a-posteriori* simulations by Whitmore *et al.* (2022). Freestream velocities with a nonreflective boundary condition are set at the top boundary. A characteristic boundary condition (NSCBC) with constant pressure is applied at the outlet ($x/L = 2.5$). The computational meshing approach is the same as in Agrawal *et al.* (2022); some details of the mesh parameters are provided in Table 1.

The experiments of Williams *et al.* (2020) and Gray *et al.* (2021) have suggested an approximate Reynolds number independence in the surface pressure distribution over the bump surface for $Re_L \geq 2 \times 10^6$. In light of this, in this work, we perform numerical experiments up to $Re_L = 10 \times 10^6$, assuming the invariance of the pressure coefficient profile with respect to the Reynolds number. Only comparisons of the surface pressure distribution are made as it is expected that the skin-friction distribution in the upstream region (nearly a zero-pressure-gradient flat-plate flow) is expected to be a function of the Reynolds number. In a prior work (Agrawal *et al.* 2022), the authors showed that for the Reynolds number $Re_L = 2 \times 10^6$ case, the skin friction compares well with the experiments. For completeness, the surface pressure coefficient (C_p) is mathematically defined as

$$\frac{C_p}{2} = \frac{p - p_{\text{ref}}}{\rho_\infty U_\infty^2}, \qquad (4.2)$$

where U_∞, p, and p_{ref} are the mean freestream velocity, wall pressure and the upstream reference pressure in the zero-pressure region of the flow, respectively.

Figure 6 (a–c) provides the predictions of the surface pressure at a given nominal grid for different values of Re_L, where at each level (e.g., coarse, medium, fine), grids are refined based on the proposed Reynolds number scaling ($Re_L^{2/3}$). When the resolution
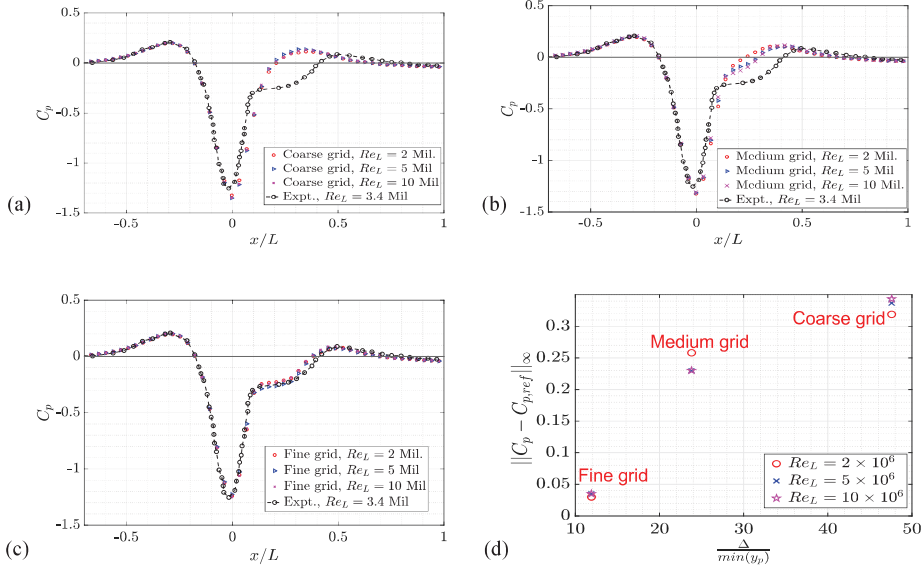
FIGURE 6. The streamwise distribution of the surface pressure coefficient, C_p, for the (a) coarse grid, (b) medium grid and (c) fine grid across $2 \times 10^6 \leq Re_L \leq 10 \times 10^6$. Note that across different Reynolds numbers, the nominal coarse, medium and fine grids are scaled in their resolution by a factor of $Re_L^{2/3}$. Subfigure (d) shows the L_∞ norm of the error in C_p for all the Reynolds number flows.

of the calculation with respect to L_p is held constant, it is apparent that predictions of WMLES at different Reynolds numbers are similar. For all the considered cases, the finest grid is required to accurately predict C_p, specifically, the flow separation ($0.1 \leq x/L \leq 0.4$). To quantify these errors, Figure 6(d) presents the L_∞ norm of the error in C_p. This norm specifically highlights the largest differences in WMLES and reference values, which occur primarily due to incorrect prediction of the extent of the separation bubble. The error values are expected to reach an asymptotic value on very coarse grids when the prediction of C_p reaches the inviscid limit (the flow remains attached and the boundary layers are sufficiently thin). The error convergence on the fine grid corresponds to a $\Delta/min(l_p) \sim 12$, which is similar to the values from the *a-priori* analysis in the preceding sections. Although not shown, limited sensitivity in the convergence behavior of WMLES upon the choice of the subgrid-scale model was observed between the dynamic Smagorinksy model (Moin *et al.* 1991) and the dynamic tensor coefficient Smagorinsky model (Agrawal *et al.* 2022). The minimum y^+ values before the separation point are approximately $y_w^+ \approx 15-20$ at the lowest, implying the simulations are not wall-resolved. Finally, an additional simulation on a very fine grid (twice as refined in each direction than the fine grid shown) for the $Re_L = 5 \times 10^6$ case confirmed that the results are grid-converged.

4.2. *WMLES of Song-Eaton diffuser*

Song & Eaton (2004) performed detailed experiments on the Reynolds number sensitivities of flow separation over a circular arc-shaped diffuser. The experiments recorded a small separation bubble with nearly Reynolds number invariant C_p distribution across a range of $1100 \leq Re_\theta^{ref} \leq 20,100$ where Re_θ^{ref} denotes the momentum-thickness-based Reynolds number at a reference station ($s/L = -2$) in the flat-plate region of the dif-
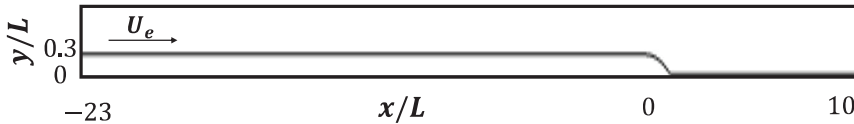
FIGURE 7. A schematic of the flow over the spanwise periodic circular arc-shaped diffuser studied by Song & Eaton (2004). The flow develops over a flat plate upstream of the arc before experiencing a favorable and then an adverse pressure gradient. The flow eventually separates at $s/L \approx 0.75$.

Mesh	N_{cv} (in millions)	Max. Δ/L	Min. Δ/L
Coarse	0.6	0.03	7.6×10^{-3}
Medium	2.2	0.03	3.8×10^{-3}
Fine	9.3	0.03	1.9×10^{-3}

TABLE 2. Mesh parameters for the inlet momentum thickness, $Re_\theta^{ref} = 3400$ case of the flow over the circular arc-shaped diffuser studied by Song & Eaton (2004). For subsequently higher Reynolds numbers, the grid is refined by modifying the background resolution (equal to max. Δ/L) by a factor of $Re^{2/3}$.

fuser. Figure 7 presents a schematic of the experimental setup. In this flow, the unsteady separation process occurs over a large portion of the arc surface, leading to the formation of intermittently attached and separated boundary layers. Radhakrishnan *et al.* (2006) performed a hybrid RANS-LES of this flow with a stochastic forcing (Keating & Piomelli 2006) to reasonably capture the separation bubble for the $Re_\theta^{ref} = 13,200$ flow, however, they employed stretched grids in the streamwise direction, with a wall-normal refinement down to $y^+ = 1$.

Table 2 presents details of the computational grids in this work. The simulation setup for this flow is very similar to the Boeing speed bump. A plug-flow is fed at the inlet ($x/L = -23$), which transitions into an equilibrium turbulent boundary layer as it develops over a long flat-plate region. The upstream length has been chosen such that simulations match the velocity profile and the Reynolds number at the reference upstream experimental station ($x/L = -2$). The outlet boundary in the simulations was extended up to $x/L = 10$ to let the flow fully recover post-reattachment. The top boundary is placed at $y/L = 2.1$ and treated with a free-slip boundary condition. The bottom wall is treated using the equilibrium wall model, and the outlet is treated with the characteristic boundary condition (NSCBC). Unlike Radhakrishnan *et al.* (2006), the grid resolution is agnostic to the separation location along the streamwise directions. Periodic boundary conditions are used along the spanwise direction with a period of 20 δ_{99}^{ref}, where δ_{99}^{ref} is the boundary layer thickness at the reference upstream station ($x/L = -2$).

In this work, we perform WMLES of all three Reynolds numbers, $Re_\theta^{ref} = 3400$, 13,200 and 20,100 considered in the experiments. Figure 8 (a–c) corresponds to the C_p distribution for three Reynolds numbers, respectively. The C_p distribution is nearly identical for all Reynolds numbers, with the flow experiencing an acceleration slightly upstream of the arc (as $x/L \to 0$). Then, as the boundary layer experiences an adverse pressure gra-
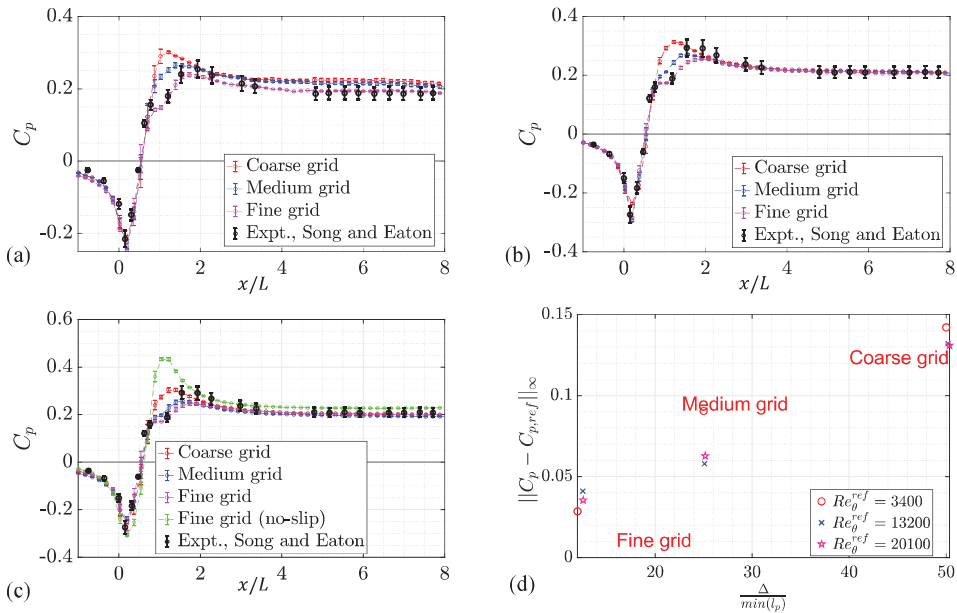
FIGURE 8. The prediction of surface pressure coefficient C_p for the flow over the Song-Eaton diffuser at (a) $Re_\theta^{ref} = 3400$, (b) $Re_\theta^{ref} = 13,200$, and (c) $Re_\theta^{ref} = 20,100$. The flow separates at $x/L \approx 0.79$ and reattaches at $x/L \approx 1.2$. Panel (d) provides the error convergence plot upon grid refinement for different Reynolds numbers.
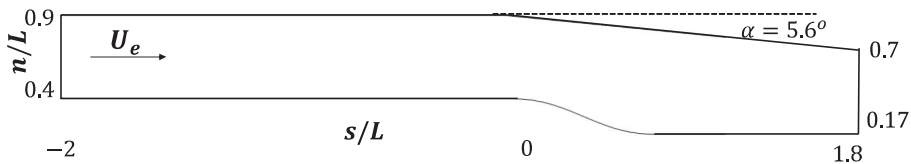

FIGURE 9. A schematic of the flow over the smooth ramp studied by Simmons (2020). The flow develops over a flat plate upstream of the ramp before separating at $x/L \approx 0.6$.

dient over the arc, a small separation occurs at $x/L \approx 0.79$. For all Reynolds numbers, the fine grid accurately captures the separation bubble and the flow recovery regions. Figure 8 also shows that at $Re_\theta = 20,100$, a fine grid simulation with no-slip boundary conditions on the bottom walls produces the inviscid C_p solution and does not predict any flow separation, which confirms the necessity of a wall model to simulate this flow at the finest grid resolution. For this flow, the performance of WMLES for coarse and medium grids varies between the lowest and the other two different Reynolds numbers, similar to the Boeing speed bump. Figure 8(d) presents the L_∞ norm of the error in the C_p, with the errors becoming small only for the finest grid. Selected sensitivity tests to the choice of the subgrid-scale model suggested no differences in the grid-point scaling with the Reynolds number.

4.3. *WMLES of Notre-Dame ramp*

Simmons (2020) performed a series of experiments on a smooth ramp over which a high–Reynolds number boundary layer (upstream reference $Re_\theta = 11,000$) exhibits a smooth-body separation; this flow is a candidate for the upcoming High-Fidelity CFD

Mesh	N_{cv} (in millions)	Max. Δ/L	Min. Δ/L
Coarse	16 Mil.	0.02	2.5×10^{-3}
Medium	64 Mil.	0.02	1.3×10^{-3}
Fine	252 Mil.	0.02	6.25×10^{-4}

TABLE 3. Mesh parameters for the inlet momentum thickness, $Re_\theta^{ref} = 11,000$ case of the flow over the smooth ramp studied by Simmons (2020). The predictions on the very fine grid confirm the grid convergence of LES.

Verification Workshop at AIAA Scitech, 2024. The top wall of the experimental setup was slightly tapered to create a pressure gradient, with the tapering angle having a significant impact on the extent of the separation (Simmons 2020). Figure 9 provides a schematic of the simulation setup that nearly reproduces the experimental wind tunnel configuration. The ramp geometry ($0 < x/L < 1$) is made from a fifth-order polynomial that smoothly joins the upstream and downstream flat plates. Three tapering angles, $\alpha = 3.2^o$, 5.6^o and 7.7^o, were studied experimentally, with the smallest angle producing the largest separation bubble and the largest angle producing a fully attached flow. In this study, we consider the $\alpha = 5.6^o$ flow, expecting that this angle will be the most challenging condition in regard to the prediction of the separation bubble.

In our computations, the inlet is fed as a plug-flow located at $s/L = -2$. The inlet is adjusted to match the experimental Reynolds number ($Re_\theta^{ref} = 11,000$) at the reference plane ($s/L = -0.75$). The top wall is located at $n/L = 0.9$, the same as the experimental domain and an equilibrium wall model is used at this boundary, since the flow is not inviscid near the tunnel wall. The bottom wall flat-plate regions and the ramp are also treated with the equilibrium wall model. The outlet boundary condition is a nonreflective characteristic boundary condition. The domain is $25\delta_{99}^{ref}$ wide in the spanwise direction. Details of the grid distribution and resolutions are provided in Table 3.

Figure 10(a) shows the C_p distribution across the grid refinement sweep. As the flow encounters the ramp, a favorable pressure gradient is experienced initially due to the tapering of the top wall that creates an inviscid flow acceleration. However, at $s/L \approx 0.2$, the adverse pressure gradient due to the ramp surface dominates and leads to the formation of a separation bubble at $s/L \approx 0.5$. In the current WMLES results, on the coarsest grid, the flow does not separate. As the grid is refined, the flow starts separating with the fine and the very fine grids providing nearly identical solutions, indicating grid convergence for these quantities. Table 3 and Figure 10(b) suggest that for the fine grid, the resolution in terms of the pressure-scaled units is of the same order as that required on the Boeing speed bump and the Song-Eaton diffuser flow.

5. Concluding Remarks

In this study, the Reynolds number scaling of the required grid points to perform wall-modeled large-eddy simulation (WMLES) of flow encountering separation is examined. A theoretical justification based on the various timescales in a nonequilibrium flow is advanced to suggest that the near-wall flow structures for an otherwise nonequilibrium flow scale as $l_p \sim Re^{-2/3}$. The same scaling is deduced based on a simplified Green's function type solution of the pressure equation around the separation point. *A-priori*
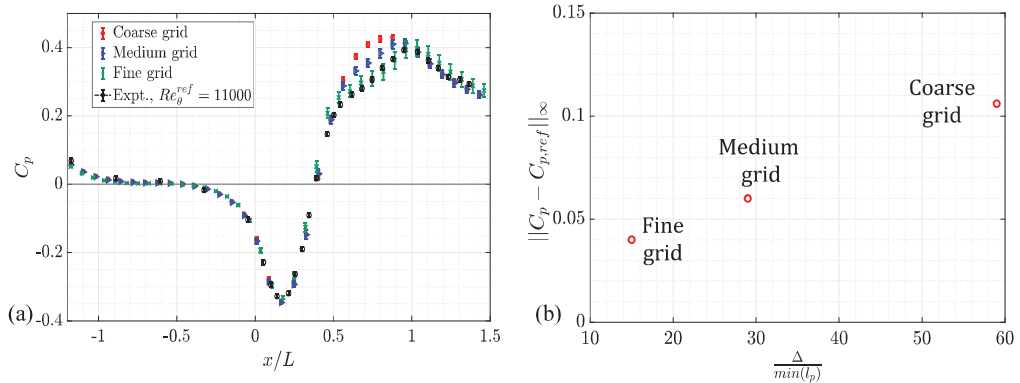
FIGURE 10. (a) The surface pressure distribution and (b) the error convergence upon grid-refinement plots for the flow over the smooth ramp designed and studied by Simmons (2020). The flow develops over a flat plate upstream of the ramp before separating at $s/L \approx 0.5$ and later reattaching with the bottom wall at $s/L \approx 0.90$.

analysis suggests that the minimum resolution required to reasonably predict (errors lower than approximately 10% in the entire domain) upon leveraging an equilibrium wall model for the shear stress is $\sim 10\, l_p$ independent of the Reynolds number and the Clauser parameter for several nonequilibrium flat plate boundary layers and airfoil flows. Several *a-posteriori* calculations are then performed to determine the accuracy of this scaling. Numerical simulations are performed and compared with experimental data for the flow over the Boeing speed bump, Song-Eaton diffuser, and the Notre Dame ramp. The results suggest that for these flows, scaling the grids (Δ) to maintain a fixed Δ/l_p results in accurate predictions of flow separation at the same "nominal" grid resolution across different Reynolds numbers. Thus, it is suggested that in more complex, three-dimensional flows, at least, locally, the grid point requirements to predict flow separation may scale as $Re^{4/3}$, which is more restrictive than the previously proposed zero pressure gradient estimates of WMLES.

Appendix I: Performance of existing nonequilibrium wall models

The results herein show that WMLES calculation with an equilibrium wall model achieves acceptable accuracy when the viscous pressure gradient length scales are resolved. As the equilibrium formulations do not include pressure gradient effects, it is possible that nonequilibrium wall models would not necessarily follow this scaling. Several nonequilibrium wall models have been proposed (Kawai & Larsson 2013; Park 2017; Zhou *et al.* 2023; Kamogawa *et al.* 2023) to account for the flow nonequilibrium by modeling the pressure gradient and convective terms either using governing equations or data-driven methods. These studies have all suggested some improvements in the *a-posteriori* WMLES predictions upon employing their respective nonequilibrium wall models over a range of mildly separated flows. Table 4 summarizes the near-wall, wall-normal grid resolution (non-dimensionalized by the viscous scale imposed by the strongest pressure gradient) required to predict the quantities of interest accurately. It is clear that for all considered flows, the resolution requirements are not too dissimilar to those required by WMLES employing the equilibrium wall model in this study. Further research may provide the Reynolds number scaling of these models, and present improvements in the $N_{cv} \sim Re^{4/3}$ cost scaling, if any.

Model Description	Flow	$\min\left(\Delta/l_p\right)$
PDE, nonequilibrium wall-model (Park 2017)	NASA Hump	≈ 16
PDE, nonequilibrium wall-model (Kawai & Asada 2013)	Airfoil	≈ 14
Reinforcement learning wall-model (Zhou *et al.* 2023)	Periodic Hill	≈ 14
ODE, nonequilibrium wall-model (Kamogawa *et al.* 2023)	Suction, blowing boundary layer	≈ 15

TABLE 4. The minimum wall normal resolutions reported for accurate prediction of quantities of interest while leveraging existing nonequilibrium wall models for a range of mildly separated flows.

Acknowledgments

REFERENCES

ADAMS, E. & JOHNSTON, J. 1988 Flow structure in the near-wall zone of a turbulent separated flow. *AIAA J.* **26**, 932–939.

AGRAWAL, R., BOSE, S. T., GRIFFIN, K. P. & MOIN, P. 2023*a* An extension of Thwaites method for turbulent boundary layers. *arXiv:2310.16337* .

AGRAWAL, R., ELNAHHAS, A. & MOIN, P. 2023*b* Wall modeled large-eddy simulations of flow over the sandia transonic hump. In *AIAA Aviation 2023 Forum*, p. 3972.

AGRAWAL, R., WHITMORE, M. P., GOC, K., BOSE, S. T. & MOIN, P. 2023*c* Reynolds number sensitivities in wall-modeled large-eddy simulation of a high-lift aircraft. *Annual Research Briefs*, Center for Turbulence Research, Stanford University, in press.

AGRAWAL, R., WHITMORE, M. P., GRIFFIN, K. P., BOSE, S. T. & MOIN, P. 2022 Non-Boussinesq subgrid-scale model with dynamic tensorial coefficients. *Phys. Rev. Fluids* **7**, 074602.

BOBKE, A., VINUESA, R., ÖRLÜ, R. & SCHLATTER, P. 2017 History effects and near equilibrium in adverse-pressure-gradient turbulent boundary layers. *J. Fluid Mech.* **820**, 667–692.

BRÈS, G. A., BOSE, S. T., EMORY, M., HAM, F. E., SCHMIDT, O. T., RIGAS, G. & COLONIUS, T. 2018 Large-eddy simulations of co-annular turbulent jet using a Voronoi-based mesh generation framework. In *2018 AIAA/CEAS Aeroacoustics Conference*, p. 3302.

CHAPMAN, D. R. 1979 Computational aerodynamics development and outlook. *AIAA J.* **17**, 1293–1313.

CHOI, H. & MOIN, P. 2012 Grid-point requirements for large eddy simulation: Chapman′s estimates revisited. *Phys. Fluids* **24**, 011702.

FU, L., KARP, M., BOSE, S. T., MOIN, P. & URZAY, J. 2021 Shock-induced heating

and transition to turbulence in a hypersonic boundary layer. *J. Fluid Mech.* **909**, A8.

GOC, K. A., LEHMKUHL, O., PARK, G. I., BOSE, S. T. & MOIN, P. 2021 Large eddy simulation of aircraft at affordable cost: a milestone in computational fluid dynamics. *Flow* **1**, E14.

GOC, K. A., MOIN, P., BOSE, S. T. & CLARK, A. M. 2023 Wind tunnel and grid resolution effects in large-eddy simulations of the high-lift common research model. *J. Aircraft* 1–13.

GRAY, P. D., GLUZMAN, I., THOMAS, F., CORKE, T., LAKEBRINK, M. & MEJIA, K. 2021 A new validation experiment for smooth-body separation. In *AIAA Aviation 2021 Forum*, p. 2810.

GRAY, P. D., GLUZMAN, I., THOMAS, F. O. & CORKE, T. C. 2022 Experimental characterization of smooth body flow separation over wall-mounted Gaussian bump. In *AIAA Scitech 2022 Forum*, p. 1209.

KAMOGAWA, R., TAMAKI, Y. & KAWAI, S. 2023 Ordinary-differential-equation-based nonequilibrium wall modeling for large-eddy simulation. *Phys. Rev. Fluids* **8**, 064605.

KAWAI, S. & ASADA, K. 2013 Wall-modeled large-eddy simulation of high Reynolds number flow around an airfoil near stall condition. *Computers & Fluids* **85**, 105–113.

KAWAI, S. & LARSSON, J. 2013 Dynamic non-equilibrium wall-modeling for large eddy simulation at high Reynolds numbers. *Physics of Fluids* **25** (1), 015105.

KEATING, A. & PIOMELLI, U. 2006 A dynamic stochastic forcing method as a wall-layer model for large-eddy simulation. *J. Turbul.* p. N12.

KIRIS, C. C., GHATE, A. S., BROWNE, O. M., SLOTNICK, J., & LARSSON, J. 2023 HLPW-4: Wall-modeled large-eddy simulation and Lattice–Boltzmann technology focus group workshop summary. *J. Aircraft* **60**, 1–23.

KIRIS, C. C., GHATE, A. S., DUENSING, J. C., BROWNE, O. M., HOUSMAN, J. A., STICH, G.-D., KENWAY, G., FERNANDES, L. S. & MACHADO, L. M. 2022 High-lift common research model: RANS, HRLES, and WMLES perspectives for CLmax prediction using LAVA. In *AIAA Scitech 2022 Forum*, p. 1554.

KIYA, M. & SASAKI, K. 1983 Structure of a turbulent separation bubble. *J. Fluid Mech.* **137**, 83–113.

LEHMKUHL, O., PARK, G. I., BOSE, S. T. & MOIN, P. 2018 Large-eddy simulation of practical aeronautical flows at stall conditions. *Proceedings of the Summer Program 2018*, Center for Turbulence Research, Stanford University pp. 87–96.

LIGHTHILL, M. J. 1953 On boundary layers and upstream influence II. supersonic flows without separation. *Proc. R. Soc. Lond. A Math.* **217**, 478–507.

LOZANO-DURÁN, A., BOSE, S. T. & MOIN, P. 2022 Performance of wall-modeled LES with boundary-layer-conforming grids for external aerodynamics. *AIAA J.* **60**, 747–766.

LOZANO-DURÁN, A., GIOMETTO, M. G., PARK, G. I. & MOIN, P. 2020 Non-equilibrium three-dimensional boundary layers at moderate Reynolds numbers. *J. Fluid Mech.* **883**, A20.

MOIN, P., SQUIRES, K., CABOT, W. & LEE, S. 1991 A dynamic subgrid-scale model for compressible turbulence and scalar transport. *Phys. Fluids A - Fluids* **3**, 2746–2757.

PARK, G. I. 2017 Wall-modeled large-eddy simulation of a high Reynolds number separating and reattaching flow. *AIAA Journal* **55**, 3709–3721.

RADHAKRISHNAN, S., KEATING, A., PIOMELLI, U. & SILVA LOPES, A. 2006 Large-

eddy simulations of high Reynolds-number flow over a contoured ramp. In *44th AIAA Aerospace Sciences Meeting and Exhibit*, p. 899.

SIMMONS, D. J. 2020 *An experimental investigation of smooth-body flow separation.* Ph.D. Thesis, University of Notre Dame.

SONG, S. & EATON, J. K. 2004 Reynolds number effects on a turbulent boundary layer with separation, reattachment, and recovery. *Exp. in fluids* **36**, 246–258.

SREENIVASAN, K. 1982 Laminarescent, relaminarizing and retransitional flows. *Acta Mech.* **44**, 1–48.

STRATFORD, B. 1959 The prediction of separation of the turbulent boundary layer. *J. Fluid Mech.* **5** (1), 1–16.

TANARRO, Á., VINUESA, R. & SCHLATTER, P. 2020 Effect of adverse pressure gradients on turbulent wing boundary layers. *Journal of Fluid Mechanics* **883**, A8.

UZUN, A. & MALIK, M. R. 2022 High-fidelity simulation of turbulent flow past Gaussian bump. *AIAA J.* **60**, 2130–2149.

VINUESA, R., NEGI, P. S., ATZORI, M., HANIFI, A., HENNINGSON, D. S. & SCHLAT-TER, P. 2018 Turbulent boundary layers around wing sections up to $Re_c = 1,000,000$. *Int. J. Heat and Fluid Flow* **72**, 86–99.

WHITMORE, M. P., S.T., B. & MOIN, P. 2022 Progress on slip wall modeled LES for predicting smooth body separation. *Annual Research Briefs*, Center for Turbulence Research, Stanford University, pp. 59–70.

WILLIAMS, O., SAMUELL, M., SARWAS, E. S., ROBBINS, M. & FERRANTE, A. 2020 Experimental study of a CFD validation test case for turbulent separated flows. In *AIAA Scitech 2020 Forum*, p. 0092.

YANG, X. I. A. & GRIFFIN, K. P. 2021 Grid-point and time-step requirements for direct numerical simulation and large-eddy simulation. *Phys. Fluids* **33**, 015108.

ZHOU, D., WHITMORE, M. P., GRIFFIN, K. P. & BAE, H. J. 2023 Large-eddy simulation of flow over Boeing Gaussian bump using multi-agent reinforcement learning wall model. In *AIAA Aviation 2023 Forum*, p. 3985.